HHS Public Access

Author manuscript

J Am Chem Soc. Author manuscript; available in PMC 2020 May 29.

Published in final edited form as:

J Am Chem Soc. 2019 November 20; 141(46): 18508–18520. doi:10.1021/jacs.9b09016.

The Myth of d^8 Copper(III)

Ida M. DiMucci[†], **James T. Lukens**[†], **Sudipta Chatterjee**[†], **Kurtis M. Carsch**[‡], **Charles J. Titus**[§], **Sang Jun Lee**[‖], **Dennis Nordlund**[‖], **Theodore A. Betley**[‡], **Samantha N. MacMillan**[†], **Kyle M. Lancaster**[*,†]

[†] Department of Chemistry and Chemical Biology, Cornell University, Baker Laboratory, 162 Sciences Drive, Ithaca, New York 14853, United States

[‡] Department of Chemistry and Chemical Biology, Harvard University, 12 Oxford Street, Cambridge, Massachusetts 02138, United States

[§] Department of Physics, Stanford University, Stanford, California 94305, United States

[‖] Stanford Synchrotron Radiation Lightsource, SLAC National Accelerator Laboratory, Menlo Park, California 94025, United States

Abstract

Seventeen Cu complexes with formal oxidation states ranging from Cu^{I} to Cu^{III} are investigated through the use of multiedge X-ray absorption spectroscopy (XAS) and density functional theory (DFT) calculations. Analysis reveals that the metal−ligand bonding in high-valent, formally Cu^{III} species is extremely covalent, resulting in Cu K-edge and $L_{2,3}$-edge spectra whose features have energies that complicate physical oxidation state assignment. Covalency analysis of the Cu $L_{2,3}$-edge data reveals that all formally Cu^{III} species have significantly diminished Cu d-character in their lowest unoccupied molecular orbitals (LUMOs). DFT calculations provide further validation of the orbital composition analysis, and excellent agreement is found between the calculated and experimental results. The finding that Cu has limited capacity to be oxidized necessitates localization of electron hole character on the supporting ligands; consequently, the physical d^8 description for these formally Cu^{III} species is inaccurate. This study provides an alternative explanation for the competence of formally Cu^{III} species in transformations that are traditionally described as metal-centered, 2-electron Cu^{I}/Cu^{III} redox processes.

Graphical Abstract

[*]**Corresponding Author** kml236@cornell.edu.

ASSOCIATED CONTENT

Supporting Information

The Supporting Information is available free of charge on the ACS Publications website at DOI: 10.1021/jacs.9b09016.

Input coordinates, multi-edge X-ray absorption spectra, and calculated spectra for each species; UV−vis, ^{1}H NMR spectra, and crystallographic data for species **14** (PDF)

The authors declare no competing financial interest.

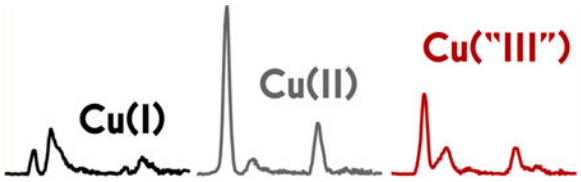

INTRODUCTION

High-valent Cu complexes are frequently proposed as key intermediates in chemical reactions pertinent to biological and synthetic catalysis.[1,2] For example, in the context of Cu-catalyzed carbon−carbon and carbon−heteroatom bond-forming reactions,[3,4] Cu^{I}/Cu^{III} redox couples are typically invoked to rationalize the competence of Cu for the two-electron bond-forming step: reductive elimination from a formally Cu^{III} center yields the final product with concomitant formation of Cu^{I}. Although Cu^{III} has yet to be definitively assigned to any redox transformation in biology, it has been implicated in silico in mechanistic studies of Cu mono-oxygenases.[5,6] In addition, some model complexes of the 1:1 Cu/O_2 adduct of the Cu monooxygenase active site have formally Cu^{III}-peroxide character, which is cited as the root of their reactivity/instability.[7] Remarkably, although high reactivity and instability typifies Cu^{III} complexes, there are now numerous reports of isolable, crystallographically characterized, and even chemically inert complexes bearing formally Cu^{III} centers.[8−10]

One such curiosity is Naumann's $[Cu(CF_3)_4]^{1-}$ ion, which forms inert, colorless crystalline salts.[8] The electronic structure of this species was investigated by Snyder, who attributed the stability of the ion to "ligand field inversion" on the basis of quantum chemical calculations.[11] Unlike a classical Werner coordination complex in which dative bonding gives rise to metal-based frontier orbitals, Snyder noted that the frontier molecular orbitals of $[Cu(CF_3)_4]^{1-}$ are dominated by ligand parentage (Figure 1), implying that the Cu center in $[Cu(CF_3)_4]^{1-}$ is better described as physically d^{10} Cu^{I}. This formulation echoes C. K. Jørgensen's efforts to rationalize the ionic roots of the oxidation state formalism with the experimental observation of $^{35,37}Cl$ hyperfine in the electron paramagnetic resonance spectrum of the Ir^{IV} ion of $[IrCl_6]^{2-}$: "Suppose that Owen and Stevens' experiment had given the result that 28% of the uncompensated spin density (of the hole) were located on Ir and 12% on each of the six Cl, one would have had a collectively oxidized set of ligands Cl_6^{5-} and the oxidation state of the central atom would have been Ir^{III}".[12] Snyder's assertion was met with fierce criticism;[13] however, application of core spectroscopies by our group experimentally validated the inverted ligand field electronic structure of $[Cu(CF_3)_4]^{1-}$ and supported the formulation of this ion as a physically Cu^{I} species.[14] Further support for this electronic structure was furnished in a recent high-resolution crystallog-raphy study.[15] The case of $[Cu(CF_3)_4]^{1-}$ is summarized in an extensive review/concept paper on ligand field inversion by Hoffmann, Alvarez, Mealli, and co-workers.[16] The inverted ligand field concept has since appeared in additional discussions of compounds bearing group 11 elements.[17−19]

Recent X-ray spectroscopic studies have challenged the notion that Cu K-edge X-ray absorption spectroscopy (XAS) diagnoses the physical d^8 Cu^{III} oxidation state. Specifically,

prior work asserted that the weak, quadrupole-allowed preedge peak assigned as the Cu 1s → Cu 3d distinguished d^9 Cu^{II} from d^8 Cu^{III}, with Cu^{II} pre-edge features occurring at 8979 ± 0.3 eV and Cu^{III} pre-edge features occurring at 8981 ± 0.5 eV.[20] Through advanced multiconfigurational ab initio calculations, Tomson, Wieghardt, and co-workers[21] demonstrated that complexes bearing Cu^{II} centers can exhibit preedge peaks in the range previously ascribed to Cu^{III}. Additionally, a recent paper by Solomon, Ghosh, Hedman, Hodgson, and co-workers[22] highlights that, in homologous, yet highly covalent, Cu^{II}/Cu^{III} systems, shifts of up to 0.8 eV may be indicative of partial ligand oxidation, as opposed to metal oxidation from Cu^{II} to Cu^{III}. Furthermore, our group[23,24] and others[25] have shown that metal K-edge XAS transitions involving ligand-localized acceptor orbitals, as well as spectral shifts arising from changes in coordination environment, can complicate metal K-edge analysis.

We now use Cu $L_{2,3}$-edge XAS in concert with experimentally calibrated electronic structure calculations to show that ligand field inversion is general to formally Cu^{III} complexes. Our reinterpretation of the electronic structures of formally Cu^{III} species relies not on XAS transition energies but rather on the fact that the electric-dipole allowed nature of Cu 2p → 3d transitions affords a direct metric of acceptor orbital 3d parentage. The lowest Ψ* acceptor orbitals probed via Cu K- and $L_{2,3}$-edge XAS comprise ligand np character (α^2), and the covalency of the Cu 3d-L interaction will change according to the following equation:

$$\Psi^* = \sqrt{1-\alpha^2}\left|\mathrm{Cu3d}\right> - \alpha\left|L\right> \quad (1)$$

Previous work by Cramer, Solomon, and co-workers[26] showed that the total integrated $L_{2,3}$-edge intensity scales proportionally with Cu 3d-character in acceptor orbitals. We now extend this methodology to a diverse library of formally Cu^{III} complexes. Cu $L_{2,3}$-edge XAS data interpretation is facilitated by DFT-restricted open-configuration interaction with singles (DFT-ROCIS) calculations, which afford an alternative to semiempirical valence-bond configuration interaction interpretations of Cu^{III} $L_{2,3}$-edge XAS data.[27] The Cu $L_{2,3}$-edge XAS data reported here are complemented by Cu K-edge XAS and, where appropriate, ligand K-edge XAS studies. Experimentally calibrated calculations described herein are then broadly extended to an expanded library of previously reported Cu^{III} species, as well as to reactive intermediates invoked in Cu^{III}-driven chemistry. A consensus emerges: physically d^8 Cu^{III} does not exist in any system considered, with perhaps the exception of $[CuF_6]^{3-}$.

Beyond examining ground-state electronic structure, we find that, where the oxidation state formalism dictates that two-electron chemistry is operative at Cu, redox neutrality at Cu is maintained. A recent computational examination of reductive elimination at formally Ni^{IV} centers by Klein and co-workers[28] reveals similar behavior—the system under investigation has an inverted ligand field, and the lower-valent, physically d^8 Ni^{II} electronic structure is maintained throughout the reaction coordinate. We anticipate that this behavior is generally operative in late, first-row transition metals, and the present work represents another step toward experimentally validating this hypothesis. In exposing the breakdown of oxidation state formalism, we highlight alternatives to conventional elementary mechanism that better

accord with experimentally grounded electronic structure. Such accuracy in this understanding may afford a firmer grasp of the reactivity capabilities of late transition metals.

MATERIALS AND METHODS

General Considerations.

Tetrahydrofuran (THF), dichloromethane, acetonitrile, *n*-pentane, and diethyl ether were dried using a JC Meyer Solvent System.[29] Acetone was dried over 4 Å molecular sieves. Dimethyl sulfoxide (DMSO), 2,2′-bipyridine (bpy), anhydrous copper dichloride ($CuCl_2$), copper dibromide ($CuBr_2$), 2-mercaptopyridine, potassium hydroxide, iodoform, tetra-*n*-butylammonium bromide, ethyl acetate, and hexane were purchased from VWR International, Sigma-Aldrich, and Fisher Scientific and used without further purification. Deuterated NMR solvents were purchased from Cambridge Isotope Laboratories and used as received. [Cu-$(MeCN)_4$](PF_6),[30] $Cs_2[CuCl_4]$ (**1**),[31] $(nmph)_2[CuCl_4]$ (**2**) (nmph = methyl(2-phenylethyl)ammonium),[32] $Cu(NH_3)_4(SO_4)$ (**3**),[33] (PPN)$[Cu(CF_3)_4]$ (**4**) (PPN = bis(triphenylphosphine)iminium),[34] Cu(bpy)$(CF_3)_3$ (**5**),[35] Cu(phen)$(CF_3)_3$ (phen = 1,10-phenanthroline) (**6**),[35] Cu(fpoh)(DMSO) (**7**) (fpoh = 2*N*(oxime),2*N*(hydrazide)), [36] Cu(fpoh) (**8**),[36] (PPh_4)[Cu(hmpb)]·$2H_2O$ (**9**) (H4hmpb = 1,2-bis(2-hydroxyl-2-methylpropanamido)benzene),[37] (PPh_4)[Cu-(phmi)] (**10**) (H_4phmi = *N,N*′−1,2-phenylenebis(2-mercapto-2-methylpropionamide)),[38] (tptm)CuCl (11) (tptm = tris(2-pyridylthio)methane),[39] [(tptm)CuCl](PF_6) (**12**),[40] (tptm)CuBr (**13**),[39] (^{EMind}L)Cu(H_2N(C_6H_4 ^{t}Bu)) (**15**)[24] (EMind = 1,1,7,7-tetraethyl-1,2,3,5,6,7-hexahydro-3,3,5,5-tetramethyl-s-indacene),[24] (^{EMind}L)Cu(HN(3,5-$(CF_3)_2C_6H_3$)) (**16**),[24] and (^{EMind}L)Cu(N-(C_6H_4^{t}Bu)) (**17**) were prepared according to literature procedures. [(tptm)CuBr](PF_6) (**14**) was prepared using an analogous method to **12**. Characterization of **14** is included in the Supporting Information. Where required, compounds were maintained under inert N_2 atmosphere using an MBraun glovebox or standard Schlenk techniques.

XAS Data Collection.

All data were measured at the Stanford Synchrotron Radiation Lightsource (SSRL) under ring conditions of 3.0 GeV and 500 mA. All air-sensitive samples were prepared in an inert-atmosphere glovebox and were measured as solids. For Cu K-edge measurements, samples were ground with boron nitride (BN) to a final concentration of 5 wt % Cu, pressed into 1 mm aluminum spacers, and sealed with 37 μm Kapton tape. For S and Cl K-edge measurements, samples were prepared by grinding to a fine powder and spreading thinly onto 38 μm low-S Mylar tape. For Cu $L_{2,3}$-edge measurements, samples were ground to a fine powder and spread in a thin layer on carbon tape affixed to an aluminum sample rod.

All Cu K-edge measurements were carried out at either SSRL beamline 7–3 or 9–3. Beamline 9–3 is equipped with a 16-pole, 2-T wiggler source, while beamline 7–3 is equipped with a 20-pole, 2-T wiggler. In both cases incident X-ray radiation was monochromated using a double Si(220) crystal monochromator. Samples were maintained at 10 K in a liquid He cryostat during data collection. Spectra were collected in fluorescence mode, with X-rays detected by a PIPS (passivated, implanted, planar silicon) detector placed

at a 90° angle to the sample. A Cu foil and a third ionization chamber upstream of the sample were used for internal energy calibration, setting the first inflection point of the Cu foil scan to 8980.3 eV. Data were collected from 8660 to 9600 eV. Four scans were measured and averaged for each compound. Spectra were processed using Sixpack[41] and Igor Pro. The region below 8970 eV was used to fit a linear background, while the region above 9000 eV was flattened with a piecewise spline and set to an average intensity of 1.0.

All S and Cl K-edge measurements were collected using beamline 4–3 equipped with a 20-pole, 2-T wiggler source. All samples were measured in a He atmosphere at room temperature in fluorescence mode using a Lytle detector. Intensity was normalized with respect to the incident beam using a He-filled ion chamber upstream of the sample. The incident beam energy was calibrated by setting the first inflection point in the S K-edge spectrum of $Na_2S_2O_3$ to 2472.02 eV and in the Cl K-edge spectrum of Cs_2CuCl_4 to 2820.2 eV. Data were collected from 2400 to 2800 eV (S) and 2720 to 3150 eV (Cl). Four scans were measured and averaged for each compound. The region below 2460 eV (S) and 2800 eV (Cl) was used to fit a linear background, and the region above 2475 eV (S) and 2830 eV (Cl) was flattened with a piecewise spline and set to an average intensity of 1. Raw data was processed using Sixpack and Igor Pro. Spectra were fit according to a pseudo-Voigt deconvolution of pre-edge and rising edge peaks with Igor 6.37.

Cu $L_{2,3}$-edge XAS measurements for all compounds were collected on beamline 10–1, equipped with a 31-pole wiggler source, a 1000 lines/mm spherical grating monochromator, and 29 μm entrance and exit slits. Data were measured by monitoring fluorescence using a transition edge sensor (TES) operated under typical conditions as described previously.[42] Raw TES data was processed into pulse heights via a matched filter,[43] and these pulse heights were calibrated by measuring the nonresonant emission from a blended powder of copper oxide. To create the Cu PFY-XAS, the measured emission was windowed between 880 and 960 eV. The signal was normalized to incident photon flux with a gold-grid reference monitor. Incident beam energy was calibrated to the L_3-edge position at 930.65 eV of a $(nmph)_2[CuCl_4]$ standard collected before and after each sample.[26] Samples were maintained at room temperature under an ultrahigh vacuum (10^{-9} Torr) during collection. Data were collected from 910.0 to 990.0 eV. Processing was carried out using PyMCA.[44] Background subtraction was achieved with E_0 set at 955 eV, by fitting a line to the pre-edge region below 920.0 eV and subtracting from the entire spectrum. The post-edge region from 975.0 to 990.0 eV was set to a flattened polynomial and normalized to 1.0. The edge jumps at L_3 and L_2 were subtracted using a statistics-sensitive nonlinear iterative peak-clipping (SNIP) algorithm[45] as implemented in PyMCA. Spectra were fit according to a pseudo-Voigt deconvolution of pre-edge and rising-edge peaks with Igor 6.37.

DFT Calculations.

Density functional theory (DFT) calculations were performed with version 4.02 of the ORCA software package.[46] Spectra were calculated from crystallographic coordinates when available or geometry-optimized coordinates using the BP86[47] functional. Single-point energies were calculated by using the B3LYP[48] functional. Cu K-edge and $L_{2,3}$-edge XAS spectra were calculated using time-dependent DFT (TDDFT)[49,50] and DFT-restricted open

configuration interaction with singles (DFT-ROCIS),[51,52] respectively, with 50-root excitations and a line-width broadening of 1 eV. Calculations with hybrid functionals used the RIJCOSX algorithm[53] to speed the calculation of Hartree−Fock exchange. The CP(PPP)[54] basis set was used for Cu with a special integration accuracy (ORCA Grid7). The scalar relativistically recontracted ZORA-def2-TZVP(-f) basis set[55] with ORCA Grid4 was used for all other atoms. Calculations included the zeroth-order regular approximation (ZORA) for relativistic effects.[56] Solvation was modeled with the conductor-like polarizable continuum model (CPCM)[57] in an infinite dielectric. Intrinsic basis bonding analysis (IBBA) of ORCA single-point DFT solutions was carried out using IboView.[58]

RESULTS AND DISCUSSION

Multiedge X-ray spectroscopic data were obtained for 17 Cu complexes, shown in Figure 2. Compounds **1−3** are covalency calibrants;[31−33] **4−14** are crystallographically characterized, formally Cu^{II} and Cu^{III} species supported by C-, S-, N-, and/or O-donor ligands.[34, 36−39,59] Complexes **15−17** comprise a homologous redox series ($Cu^{I}/Cu^{II}/Cu^{III}$) recently reported by Betley and co-workers,[24] of which **17** represents the first definitive, terminal Cu nitrenoid species, relevant for under-standing Cu-catalyzed amination and aziridination reactions.

Cu K-Edge XAS.

Normalized Cu K-edge XAS for compounds **1−17** are compiled within the Supporting Information (Figures S1−S17). The energy maxima obtained from fitting resolved pre-edge (formally 1s → 3d) and rising-edge features for the 17 species measured are provided in Table 1. Previous work by our group[14,60] and others[61,62] has shown that TDDFT accurately predicts metal and ligand K-edge XAS features, facilitating transition assignments. However, such spectral calculations require corrections of transition energies to account for large inaccuracies in core orbital potentials endemic to DFT.[50] Application of such a correction to the TDDFT-calculated energies of the complexes studied here results in excellent agreement (R^2 = 0.972) between calculated and experimental peak energies (Figure S18). This agreement suggests that DFT provides a valid means of calculating experimental spectra and orbital composition without the need for invoking multireference configuration interaction methods. We have previously estimated the global error in transition energy predictions for following such corrections as the average value of the absolute magnitude of the difference between experiment and theory after a linear correction has been performed, $|\Delta E|$.[60,63] For the currently reported K-edge XAS library, $|\Delta E|$ is 0.40 eV. Both calculated and experimental pre-edge and rising-edge features are compiled in Table 1. All species except the formally Cu^{I} species **15** display well-resolved pre-edge features in the experimental spectra. The energies of these pre-edge features range from 8977.6 (**1**) to 8981.8 eV (**4**). All species except **1**, **11−14**, and **17** have resolved rising-edge features that are predicted by TDDFT. The pre-edge features are assigned as quadrupole-allowed excitations from Cu 1s to acceptor orbitals bearing variable amounts of Cu 3d-character, and the rising-edge features are predicted by TDDFT to be excitations from Cu 1s to MOs dominated by Cu 4p character (Figures S1−S17).

The pre-edge features for the formally Cu^{III} species (**4**−**10**, **12, 14**, and **17**) investigated span a range from 8979.6 to 8981.8 eV, which exceeds the range of 8981 ± 0.5 eV conventionally held to be diagnostic of Cu^{III} species[11] Moreover, the lower end of the range approaches the 8979 ± 0.5 eV region typically ascribed to Cu^{II} [20] This observation, in combination with previous results[21,64] demonstrating that the Cu K-edge XAS spectra of Cu^{I} species with low-lying ligand π^* orbitals display a pre-edge transition similar to that observed for formally Cu^{III} species (ca. 8980.5 eV), under-scores the ambiguity that can arise when using Cu K-edge XAS pre-edge energies to assign a physical oxidation state.

Experimental Cu $L_{2,3}$-Edge XAS: Analysis of Cu 3d Contributions.

Cu $L_{2,3}$-edge XAS affords a direct means to estimate Cu 3d orbital contributions to vacant frontier MOs. Following the logic that, beyond these acceptor MOs, 3d contributions among higher-lying levels will be vanishingly small, this approach affords a means to assess d-count and the physical oxidation state of the metal center. This technique is thus a convenient means to address ligand field inversion: if the frontier orbital(s) composition comprises significantly less than 50% Cu 3d-character, then the experimental d-count will fall significantly short of that corresponding to the formal oxidation state; thus, inversion applies.

$L_{2,3}$-edge XAS of formally Cu^{III} species has been interpreted previously using the valence-bond configuration interaction (VBCI) model invoking charge-transfer multiplets.[27] Using this approach, it has been argued that the L_3 and L_2 main lines are not excitations from Cu 2p to a frontier defined by the $|3d^8>$ configuration but rather excitations to fill holes in a $|3d^9\underline{L}>$ configuration, where $\underline{L}$ denotes a vacancy in a ligand-centered MO that arises due to charge transfer. In other words, this model assigns the majority of intensity in the $L_{2,3}$ mainlines to excitations populating a $2p^53d^{10}\underline{L}$ final state, while the satellite features result from exciting to a $2p^53d^9$ final state. However, such an assignment is at odds with our prior 1s2p resonant inelastic X-ray scattering (RIXS) study of **4**, where we showed that RIXS features along the energy-transfer axis isoenergetic to the most intense $L_{2,3}$ peaks of **4** occur following resonant excitation of a Cu 1s electron into the LUMO.[14] This K-edge XAS feature is reproduced using single-determinantal TDDFT; additionally, previously reported spectroscopy oriented configuration interaction (SORCI) calculations based on a large active space (16,10) established that the ground state of 4 is effectively defined by a single configuration (Figure 3a). Meanwhile, RIXS energy transfer features isoenergetic to satellites in the $L_{2,3}$-edge XAS spectra of **4** are observed to gain maximal intensity following resonant excitation of rising-edge features in the K-edge spectrum that are assigned by TDDFT as excitations to MOs bearing appreciable Cu 4s and 4p character (Figure 3b). In other words, all features in the $L_{2,3}$-edge XAS spectrum can be reasonably assigned within a single-determinantal MO model for the electronic structure of **4**.

To further support our claim that the areas of the L_3 and L_2 mainlines, not the satellites, reflect the 3d-character defining the LUMOs/singly occupied molecular orbitals (SOMOs) in the ground-state electronic configurations, we carried out DFT-ROCIS calculations in which we removed the LUMOs/SOMOs from the acceptor orbital space (effectively removing the $2p^53d^9$ final state). After doing so, the energies and line shapes of the satellite features

remain unperturbed (Figure S19). In accord with the RIXS analysis, the satellite features can be rationalized from the DFT-based MO framework: acceptor orbitals corresponding to the satellite features are dominated by Cu 4s,4p and ligand character (Figure 3b). On the basis of this reproduction of experimental features, we assert that the $L_{2,3}$ main lines correspond to the 2p → LUMO excitations and thus afford a valid means to quantify ground-state 3d-character in the Cu species investigated.

Normalized Cu $L_{2,3}$-edge XAS for compounds **1**−**17** are included in the Supporting Information (Figures S20−S36). All species except **15** exhibit intense L_3- and L_2-edge main lines (Table 2) conventionally assigned as Cu 2p → LUMO/SOMO excitations, where the acceptor orbitals have variable Cu 3d-character. The lack of an assignable L_2-edge and the presence of a weak L_3-edge in **15** is due to a closed-shell d^{10} configuration. The L_3- and L_2-edge energies of the formally Cu^{II} species vary by only 1 eV (930.5−931.5 and 950.1−951.1 eV, respectively), while the energies for the formally Cu^{III} species vary by up to 3 eV (932.1−934.9 and 951.9−954.9 eV, respectively).

Broadly applying DFT-ROCIS with the B3LYP functional effectively reproduces both mainline and satellite Cu $L_{2,3}$-edge XAS features for all formally Cu^{III} species under consideration, without the need for invoking multiconfigurational ground states (vide infra). Overlays of calculated and experimental spectra for each species are shown in Figures S20−S36 with a strong (R^2 = 0.991) correlation between experimental and calculated $L_{2,3}$ mainline and satellite peak energies, as seen in Figure S37. Covalency analyses were carried out via consideration of mainline peak areas. $L_{2,3}$-edge areas were obtained by fitting both the L_2-and L_3-edge peaks to pseudo-Voigt line shapes and summing to obtain total areas. The approach introduced by Solomon, Cramer, and co-workers[26] was employed using a slightly expanded correlation of $L_{2,3}$-edge area to average d-orbital character in the calibration standards (**1**−**3**), whose d-orbital covalencies have been previously defined through analysis of electron paramagnetic resonance (EPR) coupling constants and ligand K-edge XAS studies (Figure 4).[65]

The average experimental Cu 3d contribution to the LUMOs/SOMOs are shown in Table 2. It should be noted that, to obtain covalency values from experimental peak areas, the number of acceptor holes must be taken into account (i.e., the total $L_{2,3}$-edge mainline peak area of a Cu species with two accessible holes will be twice the area of an analogous Cu species with only one accessible hole but with the same acceptor MO 3d parentage). After correcting for the number of accessible transitions, the SOMO and LUMO Cu 3d contributions obtained from analysis of the spectra for formally Cu^{II} and Cu^{III} complexes span a range from 15 ± 1.2% (**17**) to 72 ± 6.4% (**1**) (Table 2). Excellent agreement (R^2 = 0.982) is observed when correlating calculated percent Cu 3d-character with the experimentally obtained values (Figure 5). The Cu 3d-character of the SOMOs or LUMO generated from Löwdin analysis[66] of the quasi-restricted orbitals (QROs) used for DFT-ROCIS calculations (Table 2) yields Cu 3d percentages ranging from 16% ± 1.3 (**17**) to 72% ± 7.9 (**1**) (Figure 6); all formally Cu^{III} species have <45% Cu 3d parentage in the LUMO or SOMOs (Figure 5, blue points).

S and Cl K-edge XAS data were obtained for compounds **11−14** to quantify the remaining LUMO contributions (Figures S38−S40). S and Cl 3p contributions can be estimated using the following relationship:[67−69]

$$D_0(\mathrm{L1s} \rightarrow \Psi^*) = \alpha^2 h I_s / 3n \quad (2)$$

where D_0 is the pre-edge peak intensity, α^2 is the % S/Cl 3p, h is the number of acceptor holes, n is the number of photoexcited Cl or S atoms in the complex, and I_s is the radial dipole integral <1s|r|3p> governing the intensity of a pure S/Cl 1s → 3p excitation.

Results from the Cl K-edge XAS spectra obtained for **11** and **12** suggest only minor Cl participation in the oxidation of 11 to **12**. Using the I_s value previously obtained by Solomon and co-workers,[67] we estimate a change in the % Cl character 3p-character of the frontier orbital from only 2% to 4% upon oxidation. However, far greater changes are encountered in scrutinizing S 3p contributions: using the I_s value for S determined by Sproules, Wieghardt, and co-workers,[70] we estimated 4% and 5% S 3p-character in the LUMOs of **11** and **13**, respectively, and 23% and 21% S 3p for **12** and **14**, respectively. Ligand field inversion upon oxidation from formally Cu^{II} to Cu^{III} is evident when scrutinizing the experimentally validated frontier MO diagram generated from hybrid DFT calculations of the **11/12** and **13/14** redox series (Figures 7 and S41, respectively). DFT calculations also account for the remaining electron density of the LUMO, which is attributed to 28% C 2p-character localized to the apical carbon of the tptm ligand backbone.

Calibrated Cu Covalency Calculations: Application to Additional Reported Cu^{III} Complexes.

The number of reports of crystallographically characterized complexes bearing formally Cu^{III} complexes is steadily increasing, [2, 71,72] although only five complexes have been subject to spectroscopic characterization by Cu $L_{2,3}$-edge XAS.[24,27,67,68,73] An exhaustive $L_{2,3}$-edge XAS study of all reported Cu^{III} complexes is not feasible. However, given the fidelity between experiment and theory showcased earlier in the prediction of Cu 3d contributions to the LUMOs/SOMOs of formally Cu^{III} complexes, we have extended our calculations to explore the generality of ligand field inversion in a diverse sampling of other formally Cu^{III} complexes (Figure 8).[3,9,10,74−78] The calculated LUMOs for each species are shown in Figure 9 along with the corresponding Löwdin orbital compositions. Again, regardless of supporting ligand and geometry, our calculations show that all but one species considered ($[CuF_6]^{3-}$) possess LUMOs with <50% Cu 3d-character. The experimental Cu 3d-characters for each compound were estimated using the relationship determined via the correlation in Figure 4; again, with the exception of $[CuF_6]^{3-}$, all species exhibit inverted ligand fields.

From this analysis emerges the suggestion that electro-negative, highly oxidizing F^- ligands are required for Cu to achieve a d^8 configuration consistent with a physical Cu^{III} description. Nevertheless, even paramagnetic $S = 1$ $[CuF_6]^{3-}$ remains highly covalent, with the average calculated d-orbital contribution in each SOMO amounting to 61%; the estimated experimental value is thus 61 ± 5.0%. Even F^- may have limits to its innocence: extension to

the case of formally Cu^{IV}, $Cs_2[CuF_6]$[79] reveals that inversion will eventually manifest even in a homoleptic fluoride complex. The average Cu 3d contribution to the three vacancies in the frontier of $Cs_2[CuF_6]$ is 47%, signifying highly covalent Cu−F bonding.

Implications for Reactivity: Electron-Deficient Ligands.

To underscore the importance of the distinction between formal oxidation state and physical oxidation state as it pertains to reactivity in both biological and synthetic systems, we will first consider cases germane to C−H functionalization. In the field of Cu-catalyzed C−H bond amination and alkene aziridination, high-valent Cu terminal nitrenoid complexes have been invoked as catalytic inter-mediates for over five decades since the seminal work by Kwart and Kahn.[80–86] Although insights into the nature of a terminal Cu nitrenoid intermediate could be inferred from DFT calculations[87] or Sc^{3+}-quenched analogues,[88] the electronic structure of the proposed intermediate remained ambiguous. Recently, we prepared and isolated a bona fide copper nitrenoid complex (**17**) and established that **17** has diminished Cu character in the SOMOs (15% average). Further interrogation by N K-edge XAS and SORCI established that **17** is best characterized as a Cu^{I} triplet nitrene in contrast to a Cu^{II} iminyl or Cu^{III} imido assignment. The majority of hole character is located on the N of the nitrene (Figure 10a), thus providing unambiguous isolation and characterization of an elusive terminal Cu nitrenoid.[24] The competence of this species for C−H amination and olefin aziridination, under conditions in which the ligand sterics are attenuated and the aryl azide precursor is highly electron-deficient, is not due to an oxidized Cu center but rather to the large degree of N 2p character in the SOMOs, rendering an electron-deficient and highly reactive N center competent for room-temperature rapid amination and aziridination. Current mechanistic studies of nitrene insertion from dipyrrin-supported copper nitrenoid complexes are underway.

An example pertinent to biological systems is the formally dicopper^{III}-bis-μ-oxo $[(L^{TEED}Cu)_2(O_2)]^{2+}$ (L^{TEED} = *N,N,N′,N′*-tetraethylethylenediamine) characterized by Solo-mon and co-workers.[73] This species and related motifs are of particular interest due to the prevalence of O_2-activating Cu enzymes found in nature. Previous work by Solomon using $L_{2,3}$-edge area revealed a 40 ± 6% Cu 3d-character in the ground-state wave function of $[(L^{TEED}Cu)_2(O_2)]^{2+}$ that accords well with DFT-calculated values of 36% and 40% Cu character in the LUMO and LUMO+1, respectively.[73] Our own DFT calculations found 40% and 41% Cu character in the LUMO and LUMO+1, respectively (Figure 10b). The remaining ca. 60% hole character is distributed between the two bridging O^{2-} and ligating N atoms that mix with the two Cu d_{x2-y2} centers in an antibonding fashion. Analogous to the nitrene case discussed earlier, the large degree of O 2p contribution into the LUMO/LUMO +1 suggests that $[(L^{TEED}Cu)_2(O_2)]^{2+}$ should be highly oxidizing due to the presence of e^- deficient O^{2-} ligands. Indeed, this complex is capable of C−H and C−F bond activation as well as aromatic hydroxylation.[89–91]

Rendering ligands subvalent where donor atoms feature incomplete octets through oxidation of coordination complexes is gaining traction as a strategy to tune reactivity.[92] Recently, we compared the electronic structures and C−H amination reactivity profiles of dipyrrin-supported high-spin ferric alkyl and aryl imido complexes, (^{Ar}L)Fe(NAd) and

(^{Ar}L)Fe(N($C_6H_4{}^tBu$)) (^{Ar}L = 5-mesityl-1,9-(2,4,6-$Ph_3C_6H_2$)-dipyrrin), with their one-electron oxidized congeners.[62] N K-edge XAS and Mössbauer spectroscopy reveal that the oxidation is localized on the nitrenoid fragment and the metal ion remains in the ferric oxidation state upon chloride ligation. Oxidation of the imide to iminyl lowers the activation barrier to C−H amination of toluene by 20% in the case of the aryl imido/iminyl pair and 40% in the alkyl imido/iminyl pair. N K-edge XAS reveals far greater N-localized hole character in the alkyl iminyl (Figure 11a) compared to the aryl iminyl (Figure 11b), offering an explanation for enhanced reactivity. These examples further emphasize the importance of holistically mapping redox loci to gain deeper understanding of reactivities.

Implications for Reactivity: Reductive Elimination.

High-valent Cu is commonly invoked in organocuprate reactivity, where formal oxidative addition/reductive elimination is thought to proceed via the accessible $Cu^{I/III}$ redox pair.[2,71] In an elegant example of such chemistry, Liu, Cao, Goddard, and co-workers[3] recently reported facile C_{sp3}−C_{sp3} bond formation from $[Cu(alkyl)(CF_3)_3]^{1-}$ to form alkyl-CF_3 and $[Cu(CF_3)_2]^{1-}$ products. This activity is in stark contrast to the decidedly inert $[Cu(CF_3)_4]^{1-}$ ion that has served as a focal point in the discussion of inverted ligand fields. Computational analysis by the aforementioned authors[3] suggests that C−C bond formation from $[Cu(alkyl)(CF_3)_3]^{1-}$ proceeds predominantly via a concerted reductive elimination pathway. Curiously, however, they noted a mere 0.5 electron change at the Cu centers during this transformation.

Klein and co-workers[28] invoke ligand field inversion to rationalize the C−CF_3 bond formation of formally Ni^{IV} centers reported by Sanford and co-workers.[93] Although ligand field inversion in these systems awaits experimental validation, through intrinsic bond orbital (IBO) analysis, Klein and co-workers assert that the C−C bond-forming event proceeds without redox participation of Ni the Ni center remains effectively Ni^{II} throughout the reaction. They attribute this reactivity to attack of anionic CF_3 on a masked electrophilic aryl cation, where the electron deficiency of the arene is a consequence of the ligand field inversion or, in their parlance, "σ-non-innocence."

We have carried out a similar analysis of the Liu report on $[Cu(benzyl)(CF_3)_3]^{1-}$ and have found a striking similarity to the Klein report. Importantly, it also affords a rationale for the contrasting reactivities of $[Cu(CF_3)_4]^{1-}$ and the $[Cu(alkyl)\text{-}(CF_3)_3]^{1-}$ derivatives. Our experimentally calibrated DFT approach discussed earlier yields an inverted electronic structure for $[Cu(benzyl)(CF_3)_3]^{1-}$. Intrinsic basis bonding analysis (IBBA)[58] yields a charge of +1.01 on Cu with a d-count of 9.372 (Figure 12a). Extending this analysis to the reductive elimination transition state reported by Liu and co-workers,[3] we find a charge of +0.80 and a d-count of 9.587. Finally, the $[Cu(CF_3)_2]^{1-}$ product has a charge of +0.45 on Cu and a d-electron count of 9.686. Akin to Ni in the Klein study, Cu remains effectively redox-neutral, undergoing a dramatically smaller change in electron count than expected for a formal reductive elimination. In contrast to Klein, however, we contend that reactivity could be attributed to negative charge on the benzyl C (−0.566 e), which in turn is attracted to either of the cis-oriented, positively charged (+0.398/0.409 e) C's of the CF_3 involved in the bond-forming reaction. Such an electrostatic driving force is not available to $[Cu(CF_3)_4]^{1-}$, as all of the C atoms are positively charged (+0.420 e) (Figure 12b). Thus, this Cu system

could represent another case where bond formation is largely the domain of the coordinated ligands, while the metal serves to modulate the charge of the coordinated ligands.[94–96] The brunt of oxidation or hole character is borne by the ligands, rendering them electron-deficient, and thus permitting concerted formation of bonds between masked radical-like species.

CONCLUSION

This study details spectroscopic and computational analysis of a range of complexes containing Cu that, when described by formal oxidation state counting rules, exist in the +3 state. Through direct experimental determination of Cu and ligand character ground-state covalency values, we have shown that metal−ligand bonding exists on a spectrum of covalency ranging from that of a classical dative bond in a Werner ligand field to that of a fully inverted ligand field. Cu K-edge and $L_{2,3}$-edge features reveal no regions that are diagnostic of the Cu^{III} oxidation state.

Although understood as formalism and thus not necessarily a definitive assignment of electron density, the rigid application of formal oxidation state decidedly breaks down for late, first-row complexes. This result is not unanticipated but rather holds as a consequence of Pauling's electroneutrality principle[95,96] large charges will not accumulate at atoms that can be considered intermediate in electronegativity, i.e., the late metals. Moreover, the rising effective nuclear charges exhibited on valence electrons by late transition metal nuclei should manifest in lower limits to the physical oxidation states exhibited by these elements.[94]

The complexes studied here represent numerous examples of where this results in inverted ligand fields, suggesting that the originally discovered inverted nature of $[Cu(CF_3)_4]^{1-}$ is not unique and that ligand field inversion is observed in species with diverse coordination environments. In fact, the description of physical d^8 Cu^{III} in any case is likely unjustified, with the exception perhaps of the aforementioned $[CuF_6]^{3-}$. The persistence of Cu for remaining in low oxidation states is pertinent in both biological and synthetic systems and will inform further studies on model systems and catalyst elaboration. This study establishes the foundation for our ongoing efforts to uncover inverted ligand fields in other high-valent, first-row transition metals including Ni and Co.

Extending analysis to reductive elimination from formally Cu^{III} centers underscores the rift between formalism and scrutable electronic structure. Electronic structure analysis affords refined understanding of the origins of the C−C bond-forming reactivity of $[Cu(benzyl)(CF_3)_3]^{1-}$ as contrasted to inert $[Cu(CF_3)_4]^{1-}$. We anticipate that experimentally evaluating electronic structures will highlight the generality of ligand involvement in reactions typically attributed to high-valent metal centers. This analysis has the potential to inspire the development of new motifs and the discovery of new reaction pathways and mechanisms in group transfer.

Supplementary Material

Refer to Web version on PubMed Central for supplementary material.

ACKNOWLEDGMENTS

We thank Profs. Roald Hoffmann, David Collum, Song Lin, and Jason Shearer for valuable discussions and critical reads of this manuscript. K.M.L. acknowledges NSF (CHE-1454455) and the A. P. Sloan Foundation for support. T.A.B. acknowledges a grant from the NIH (GM-115815), the Dreyfus Foundation (Teacher-Scholar Award), and Harvard University. K.M.C. acknowledges the Fannie & John Hertz Foundation and the National Science Foundation for financial support of this research. XAS data were obtained at SSRL, which is supported by the U.S. Department of Energy, Office of Science, Office of Basic Energy Sciences under Contract no. DE-AC02–76SF00515. The SSRL Structural Molecular Biology Program is supported by the Department of Energy's Office of Biological and Environmental Research and by NIH/HIGMS (including P41GM103393). The work at SSRL was also supported by the U.S. Department of Energy Office of Basic Energy Sciences proposal no. 100487.

REFERENCES

(1). Keown W; Gary JB; Stack TD High-valent copper in biomimetic and biological oxidations. J. Biol. Inorg. Chem. 2017, 22, 289–305. [PubMed: 27909921]

(2). Hickman AJ; Sanford MS High-valent organometallic copper and palladium in catalysis. Nature 2012, 484, 177–185. [PubMed: 22498623]

(3). Paeth M; Tyndall SB; Chen LY; Hong JC; Carson WP; Liu X; Sun X; Liu J; Yang K; Hale EM; Tierney DL; Liu B; Cao Z; Cheng MJ; Goddard WA 3rd; Liu W Csp3-Csp3 Bond-Forming Reductive Elimination from Well-Defined Copper(III) Complexes. J. Am. Chem. Soc. 2019, 141, 3153–3159. [PubMed: 30678456]

(4). Tang X; Wu W; Zeng W; Jiang H Copper-Catalyzed Oxidative Carbon-Carbon and/or Carbon-Heteroatom Bond Formation with O_2 or Internal Oxidants. Acc. Chem. Res. 2018, 51, 1092–1105. [PubMed: 29648789]

(5). Abad E; Rommel JB; Kastner J Reaction mechanism of the bicopper enzyme peptidylglycine alpha-hydroxylating monooxygenase. J. Biol. Chem. 2014, 289, 13726–13738. [PubMed: 24668808]

(6). Cao L; Caldararu O; Rosenzweig AC; Ryde U Quantum Refinement Does Not Support Dinuclear Copper Sites in Crystal Structures of Particulate Methane Monooxygenase. Angew. Chem., Int. Ed. 2018, 57, 162–166.

(7). Elwell CE; Gagnon NL; Neisen BD; Dhar D; Spaeth AD; Yee GM; Tolman WB Copper-Oxygen Complexes Revisited: Structures, Spectroscopy, and Reactivity. Chem. Rev. 2017, 117, 2059–2107. [PubMed: 28103018]

(8). Naumann D; Roy T; Tebbe KF; Crump W Synthesis and structure of surprisingly stable tetrakis(trifluoromethyl)cuperate(III) salts. Angew. Chem., Int. Ed. 1993, 32, 1482–1483.

(9). Maurya YK; Noda K; Yamasumi K; Mori S; Uchiyama T; Kamitani K; Hirai T; Ninomiya K; Nishibori M; Hori Y; Shiota Y; Yoshizawa K; Ishida M; Furuta H Ground-State Copper(III) Stabilized by N-Confused/N-Linked Corroles: Synthesis, Characterization, and Redox Reactivity. J. Am. Chem. Soc. 2018, 140, 6883–6892. [PubMed: 29749234]

(10). Yao B; Wang DX; Huang ZT; Wang MX Room-temperature aerobic formation of a stable aryl-Cu(III) complex and its reactions with nucleophiles: highly efficient and diverse arene C-H functionalizations of azacalix[1]arene[3]pyridine. Chem. Commun. 2009, 2899–2901.

(11). Snyder JP Elusiveness of Cu(III) Complexation: Preference for Trifluoromethyl Oxidation in the Formation of [CuI(CF3)4]− Salts. Angew. Chem., Int. Ed. 1995, 34, 80–81.

(12). Jørgensen CK Differences between the four halide ligands, and discussion remarks on trigonal-bipyramidal complexes, on oxidation states, and on diagonal elements of one-electron energy. Coord. Chem. Rev. 1966, 1, 164–178.

(13). Kaupp M; von Schnering HG Formal Oxidation State versus Partial Charge - A Comment. Angew. Chem., Int. Ed. 1995, 34, 986–986.

(14). Walroth RC; Lukens JT; MacMillan SN; Finkelstein KD; Lancaster KM Spectroscopic Evidence for a 3d(10) Ground State Electronic Configuration and Ligand Field Inversion in [Cu(CF3)4]1−. J. Am. Chem. Soc. 2016, 138, 1922–31. [PubMed: 26844693]

(15). Gao C; Macetti G; Overgaard J Experimental X-ray Electron Density Study of Atomic Charges, Oxidation States, and Inverted Ligand Field in [Cu(CF3)4]1−. Inorg. Chem. 2019, 58, 2133–2139. [PubMed: 30645110]

(16). Hoffmann R; Alvarez S; Mealli C; Falceto A; Cahill TJ 3rd; Zeng T; Manca G From Widely Accepted Concepts in Coordination Chemistry to Inverted Ligand Fields. Chem. Rev. 2016, 116, 8173–8192. [PubMed: 27398715]

(17). Nelson HD; Hinterding SOM; Fainblat R; Creutz SE; Li X; Gamelin DR Mid-Gap States and Normal vs Inverted Bonding in Luminescent Cu^{+}- and Ag^{+}-Doped CdSe Nanocrystals. J. Am. Chem. Soc. 2017, 139, 6411–6421. [PubMed: 28421742]

(18). Ruccolo S; Rauch M; Parkin G Tris[(1-isopropylbenzimidazol-2-yl)dimethylsilyl]methyl metal complexes, [TismPr(i)Benz]M: a new class of metallacarbatranes, isomerization to a tris(N-heterocyclic carbene) derivative, and evidence for an inverted ligand field. Chem. Sci. 2017, 8, 4465–4474. [PubMed: 30155219]

(19). Baya M; Joven-Sancho DMS; Alonso PJ; Orduna J; Menjon B M-C Bond Homolysis in Coinage-Metal [M(CF3)4]1− Derivatives. Angew. Chem., Int. Ed. 2019, 131, 10059–10063.

(20). DuBois JL; Mukherjee P; Stack TDP; Hedman B; Solomon EI; Hodgson KO A Systematic K-edge X-ray Absorption Spectroscopic Study of Cu(III) Sites. J. Am. Chem. Soc. 2000, 122, 5775–5787.

(21). Tomson NC; Williams KD; Dai X; Sproules S; DeBeer S; Warren TH; Wieghardt K Re-evaluating the Cu K pre-edge XAS transition in complexes with covalent metal-ligand interactions. Chem. Sci. 2015, 6, 2474–2487. [PubMed: 29308158]

(22). Lim H; Thomas KE; Hedman B; Hodgson KO; Ghosh A; Solomon EI X-ray Absorption Spectroscopy as a Probe of Ligand Noninnocence in Metallocorroles: The Case of Copper Corroles. Inorg. Chem. 2019, 58, 6722–6730. [PubMed: 31046257]

(23). Walroth RC; Uebler JW; Lancaster KM Probing Cu(I) in homogeneous catalysis using high-energy-resolution fluorescence-detected X-ray absorption spectroscopy. Chem. Commun. 2015, 51, 9864–9867.

(24). Carsch KM; DiMucci IM; Iovan DA; Li A; Zheng S; Titus CJ; Lee SJ; Irwin KD; Nordlund D; Lancaster KM; Betley TA Synthesis of a copper−supported triplet nitrene complex pertinent to copper−catalyzed amination. Science 2019, 365, 1138–1143. [PubMed: 31515388]

(25). Kau LS; Spira-Solomon DJ; Penner-Hahn JE; Hodgson KO; Solomon EI X-ray absorption edge determination of the oxidation state and coordination number of copper. Application to the type 3 site in Rhus vernicifera laccase and its reaction with oxygen. J. Am. Chem. Soc. 1987, 109, 6433–6442.

(26). George SJ; Lowery MD; Solomon EI; Cramer SP Copper L-edge spectral studies: a direct experimental probe of the ground-state covalency in the blue copper site in plastocyanin. J. Am. Chem. Soc. 1993, 115, 2968–2969.

(27). Sarangi R; Aboelella N; Fujisawa K; Tolman WB; Hedman B; Hodgson KO; Solomon EI X-ray absorption edge spectroscopy and computational studies on LCuO2 species: Super-oxide-Cu(II) versus peroxide-Cu(III) bonding. J. Am. Chem. Soc. 2006, 128, 8286–8296. [PubMed: 16787093]

(28). Steen JS; Knizia G; Klein J Sigma-Noninnocence Masked Phenyl Cation Transfer at Formal Ni(IV). Angew. Chem., Int. Ed. 2019, 58, 13133–13139.

(29). Pangborn AB; Giardello MA; Grubbs RH; Rosen RK; Timmers FJ Safe and Convenient Procedure for Solvent Purification. Organometallics 1996, 15, 1518–1520.

(30). Baxter AC; Cameron JH; McAuley A; McLaren FM; Winfield JM The preperation of Copper(II) and Copper(I) salts in acetonitrile using group VA and VB pentafluorides. J. Fluorine Chem. 1977, 10, 289–298.

(31). Helmholz L; Kruh RF The Crystal Structure of Cesium Chlorocuprate, Cs_2CuCl_4, and the Spectrum of the Chlorocuprate Ion. J. Am. Chem. Soc. 1952, 74, 1176–1181.

(32). Hitchman MA; Cassidy PJ Polarized crystal spectrum of bis(methylphenethylammonium) tetrachlorocuprate(II): analysis of the energies, vibrational fine structure, and temperature dependence of the ″d-d″ transitions of the planar tetrachlorocuprate(2-) ion. Inorg. Chem. 1979, 18, 1745–1754.

(33). Mazzi F The crystal structure of cupric tetrammine sulfate monohydrate Cu(NH3)4SO4·H2O. Acta Crystallogr. 1955, 8, 137–141.

(34). Romine AM; Nebra N; Konovalov AI; Martin E; Benet-Buchholz J; Grushin VV Easy access to the copper(III) anion [Cu(CF3)4]1−. Angew. Chem., Int. Ed. 2015, 54, 2745–2759.

(35). Zhang SL; Bie WF Isolation and characterization of copper(III) trifluoromethyl complexes and reactivity studies of aerobic trifluoromethylation of arylboronic acids. RSC Adv. 2016, 6, 70902–70906.

(36). Fritsky IO; Kozlowski H; Kanderal OM; Haukka M; Swiatek-Kozlowska J; Gumienna-Kontecka E; Meyer F Efficient stabilization of copper(III) in tetraaza pseudo-macrocyclic oxime-and-hydrazide ligands with adjustable cavity size. Chem. Commun. 2006, 4125–4127.

(37). Anson FC; Collins TJ; Richmond TG; Santarsiero BD; Toth JE; Treco BGRT Highly stabilized copper(III) complexes. J. Am. Chem. Soc. 1987, 109 (10), 2974–2979.

(38). Hanss J; Kruger HJ The First Stable Copper(III) Complex Containing Aliphatic Thiolates as Ligands: Structural and Spectroscopic Evidence for CuII and CuIII Ions in Complexes with Square-Planar CuN2S2 Coordination Environments. Angew. Chem., Int. Ed. Engl. 1996, 35, 2827–2830.

(39). Miyamoto R; Santo R; Matsushita T; Nishioka T; Ichimura A; Teki Y; Kinoshita I A complete series of copper(II) halide complexes (X = F, Cl, Br, I) with a novel Cu(II)-C(sp3) bond. Dalton Trans. 2005, 3179–3186. [PubMed: 16172643]

(40). Santo R; Miyamoto R; Tanaka R; Nishioka T; Sato K; Toyota K; Obata M; Yano S; Kinoshita I; Ichimura A; Takui T Diamagnetic-paramagnetic conversion of tris(2-pyridylthio)-methylcopper(III) through a structural change from trigonal bipyramidal to octahedral. Angew. Chem., Int. Ed. 2006, 45 (45), 7611–4.

(41). Webb S Sixpack: Sam's Interface for XAS Package; https://www.sams-xrays.com/sixpack.

(42). Lee SJ Soft X-ray spectroscopy with Transition-Edge Sensor technology at Stanford Synchrotron Radiation Lightsource Beamline. Rev. Sci. Instrum. 2019, 90, 113101.

(43). Fowler JW; Alpert BK; Doriese WB; Joe YI; O'Neil GC; Ullom JN; Swetz DS The practice of pulse processing. J. Low Temp. Phys. 2016, 184, 374–381.

(44). Solé VA; Papillon E; Cotte M; Walter P; Susini J A multiplatform code for the analysis of energy-dispersive X-ray fluorescence spectra. Spectrochim. Acta, Part B 2007, 62, 63–68.

(45). Morhac M; Matousek V Peak Clipping Algorithms for Background Estimation in Spectroscopic Data. Appl. Spectrosc. 2008, 62, 91–106. [PubMed: 18230214]

(46). Neese F The ORCA program system. WIREs Comput. Mol. Sci. 2012, 2, 73–78.

(47). Perdew JP Density-functional approximation for the correlation energy of the inhomogeneous electron gas. Phys. Rev. B: Condens. Matter Mater. Phys. 1986, 33, 8822–8824.

(48). Stephens PJ; Devlin FJ; Chabalowski CF; Frisch MJ Ab Initio Calculation of Vibrational Absorption and Circular Dichroism Spectra Using Density Functional Force Fields. J. Phys. Chem. 1994, 98, 11623–11627.

(49). Gross EKU; Kohn W Time-Dependent Density-Functional Theory. Adv. Quantum Chem. 1990, 21, 255–291.

(50). Debeer George S; Neese F Calibration of scalar relativistic density functional theory for the calculation of sulfur K-edge X-ray absorption spectra. Inorg. Chem. 2010, 49, 1849–1853. [PubMed: 20092349]

(51). Roemelt M; Maganas D; DeBeer S; Neese F A combined DFT and restricted open-shell configuration interaction method including spin-orbit coupling: application to transition metal L-edge X-ray absorption spectroscopy. J. Chem. Phys. 2013, 138, 204101−204122.

(52). Roemelt M; Neese F Excited states of large open-shell molecules: an efficient, general, and spin-adapted approach based on a restricted open-shell ground state wave function. J. Phys. Chem. A 2013, 117, 3069–3083. [PubMed: 23510206]

(53). Neese F; Wennmohs F; Hansen A; Becker U Efficient, approximate and parallel Hartree−Fock and hybrid DFT calculations. A 'chain-of-spheres' algorithm for the Hartree−Fock exchange. Chem. Phys. 2009, 356, 98–109.

(54). Neese F Prediction and interpretation of the ^{57}Fe isomer shift in Mössbauer spectra by density functional theory. Inorg. Chim. Acta 2002, 337, 181–192.

(55). Weigend F; Ahlrichs R Balanced basis sets of split valence, triple zeta valence and quadruple zeta valence quality for H to Rn: Design and assessment of accuracy. Phys. Chem. Chem. Phys. 2005, 7, 3297–3305. [PubMed: 16240044]

(56). van Lenthe E; van der Avoird A; Wormer PES Density functional calculations of molecular hyperfine interactions in the zero order regular approximation for relativistic effects. J. Chem. Phys. 1998, 108, 4783–4796.

(57). Klamt A; Schuurmann G COSMO: A new approach to dielectric screening in solvents with explicit expressions for the screening energy and its gradient. J. Chem. Soc., Perkin Trans. 2 1993, 799–805.

(58). Knizia G Intrinsic Atomic Orbitals: An Unbiased Bridge between Quantum Theory and Chemical Concepts. J. Chem. Theory Comput. 2013, 9, 4834–4843. [PubMed: 26583402]

(59). Morimoto H; Tsubogo T; Litvinas ND; Hartwig JF A broadly applicable copper reagent for trifluoromethylations and perfluoroalkylations of aryl iodides and bromides. Angew. Chem., Int. Ed. 2011, 50, 3793–3798.

(60). Lukens JT; DiMucci IM; Kurogi T; Mindiola DJ; Lancaster KM Scrutinizing metal-ligand covalency and redox non-innocence via nitrogen K-edge X-ray absorption spectroscopy. Chem. Sci. 2019, 10, 5044–5055. [PubMed: 31183055]

(61). DeBeer George S; Petrenko T; Neese F Prediction of iron K-edge absorption spectra using time-dependent density functional theory. J. Phys. Chem. A 2008, 112, 12936–12943. [PubMed: 18698746]

(62). Wilding MJT; Iovan DA; Wrobel AT; Lukens JT; MacMillan SN; Lancaster KM; Betley TA Direct Comparison of C-H Bond Amination Efficacy through Manipulation of Nitrogen-Valence Centered Redox: Imido versus Iminyl. J. Am. Chem. Soc. 2017, 139, 14757–14766. [PubMed: 28937756]

(63). Lancaster KM; Finkelstein KD; DeBeer S K-β X-ray emission spectroscopy offers unique chemical bonding insights: revisiting the electronic structure of ferrocene. Inorg. Chem. 2011, 50, 6767–6774. [PubMed: 21692497]

(64). Walroth RC; Miles KC; Lukens JT; MacMillan SN; Stahl SS; Lancaster KM Electronic Structural Analysis of Copper(II)-TEMPO/ABNO Complexes Provides Evidence for Copper(I)-Oxoammonium Character. J. Am. Chem. Soc. 2017, 139, 13507–13517. [PubMed: 28921958]

(65). Gewirth AA; Cohen SL; Schugar HJ; Solomon EI Spectroscopic and theoretical studies of the unusual EPR parameters of distorted tetrahedral cupric sites: correlations to X-ray spectral features of core levels. Inorg. Chem. 1987, 26, 1133–1146.

(66). Löwdin PO Quantum Theory of Many-Particle Systems. I. Physical Interpretations by Means of Density Matrices, Natural Spin-Orbitals, and Convergence Problems in the Method of Configurational Interaction. Phys. Rev. 1955, 97 (6), 1474–1489.

(67). Ray K; Debeer George S; Solomon EI; Wieghardt K; Neese F Description of the ground-state covalencies of the bis(dithiolato) transition-metal complexes from X-ray absorption spectroscopy and time-dependent density-functional calculations. Chem. - Eur. J. 2007, 13, 2783–2797. [PubMed: 17290468]

(68). Sarangi R; DeBeer George S; Rudd DJ; Szilagyi RK; Ribas X; Rovira C; Almeida M; Hodgson KO; Hedman B; Solomon EI Sulfur K-edge X-ray absorption spectroscopy as a probe of ligand-metal bond covalency: metal vs ligand oxidation in copper and nickel dithiolene complexes. J. Am. Chem. Soc. 2007, 129, 2316–2326. [PubMed: 17269767]

(69). Glaser T; Hedman B; Hodgson KO; Solomon EI Ligand K-Edge X-ray Absorption Spectroscopy: A Direct Probe of Ligand−Metal Covalency. Acc. Chem. Res. 2000, 33, 859–868. [PubMed: 11123885]

(70). Sproules S; Weyhermuller T; Goddard R; Wieghardt K The rhenium tris(dithiolene) electron transfer series: calibrating covalency. Inorg. Chem. 2011, 50, 12623–12631. [PubMed: 22074340]

(71). Casitas A; Ribas X The role of organometallic copper(III) complexes in homogeneous catalysis. Chem. Sci. 2013, 4, 2301–2318.

(72). Melnik M; Kabesova M Copper(III) Coordination compounds: Classification and analysis of crystallographic structural data. J. Coord. Chem. 2000, 50, 323–338.

(73). Qayyum MF; Sarangi R; Fujisawa K; Stack TD; Karlin KD; Hodgson KO; Hedman B; Solomon EI L-edge X-ray absorption spectroscopy and DFT calculations on Cu2O2 species: direct electrophilic aromatic attack by side-on peroxo bridged dicopper(II) complexes. J. Am. Chem. Soc. 2013, 135, 17417–17431. [PubMed: 24102191]

(74). Hanss J; Beckmann A; Kruger H-J Stablization of Copper(III) Ions with Deprotonated Hydroxylaminoamide Ligands: Synthesis, Structures, and Electronic Properties of Copper(II) and Copper(III) Complexes. Eur. J. Inorg. Chem. 1999, 1999, 163–172.

(75). Ribas X; Jackson DA; Donnadieu B; Mahia J; Parella T; Xifra R; Hedman B; Hodgson KO; Llobet A; Stack TDP Aryl C-H Activation by Cu^{II} To Form an Organometallic Aryl-Cu^{III} Species: A Novel Twist on Copper Dispropotionation. Angew. Chem., Int. Ed. 2002, 41, 2991–2994.

(76). Casitas A; King AE; Parella T; Costas M; Stahl SS; Ribas X Direct observation of CuI/CuIII redox steps relevant to Ullmann-type coupling reactions. Chem. Sci. 2010, 1, 326–330.

(77). Chang HC; Lo FC; Liu WC; Lin TH; Liaw WF; Kuo TS; Lee WZ Ambient Stable Trigonal Bipyramidal Copper(III) Complexes Equipped with an Exchangeable Axial Ligand. Inorg. Chem. 2015, 54, 5527–5533. [PubMed: 25993313]

(78). Liu L; Zhu M; Yu HT; Zhang WX; Xi Z Organocopper(III) Spiro Complexes: Synthesis, Structural Characterization, and Redox Transformation. J. Am. Chem. Soc. 2017, 139, 13688–13691. [PubMed: 28933865]

(79). Allen GC; Warren KD Electronic spectra of the hexafluoronickelate (III), hexafluorocuprate (III), and hexafluoroargentate(III) anions. Inorg. Chem. 1969, 8, 1895–1901.

(80). Bakhoda AG; Jiang Q; Bertke JA; Cundari TR; Warren TH Elusive Terminal Copper Arylnitrene Intermediates. Angew. Chem., Int. Ed. 2017, 56, 6426–6430.

(81). Badiei YM; Dinescu A; Dai X; Palomino RM; Heinemann FW; Cundari TR; Warren TH Copper-nitrene complexes in catalytic C-H amination. Angew. Chem., Int. Ed. 2008, 47, 9961–9964.

(82). Aguila MJ; Badiei YM; Warren TH Mechanistic insights into C-H amination via dicopper nitrenes. J. Am. Chem. Soc. 2013, 135, 9399–9406. [PubMed: 23656170]

(83). Kwart H; Khan AA Copper-Catalyzed Decomposition of Benzenesulfonyl Azide in Cyclohexane. J. Am. Chem. Soc. 1967, 89, 1951–1953.

(84). Li Z; Quan RW; Jacobsen EN Mechanism of the (Diimine)copper-Catalyzed Asymmetric Aziridination of Alkenes, Nitrene Transfer via Ligand-Accelerated Catalysis. J. Am. Chem. Soc. 1995, 117, 5889–5890.

(85). Gephart RT; Warren TH Copper-Catalyzed sp3 C−H Amination. Organometallics 2012, 31, 7728–7752.

(86). Bakhoda AG; Jiang Q; Badiei YM; Bertke JA; Cundari TR; Warren TH Copper-Catalyzed C(sp^3)-H Amidation: Sterically Driven Primary and Secondary C-H Site-Selectivity. Angew. Chem., Int. Ed. 2019, 58, 3421–3425.

(87). Corona T; Ribas L; Rovira M; Farquhar ER; Ribas X; Ray K; Company A Characterization and Reactivity Studies of a Terminal Copper−Nitrene Species. Angew. Chem., Int. Ed. 2016, 55, 14005–14008.

(88). Kundu S; Miceli E; Farquhar E; Pfaff FF; Kuhlmann U; Hildebrandt P; Braun B; Greco C; Ray K Lewis Acid Trapping of an Elusive Copper−Tosylnitrene Intermediate Using Scandium Triflate. J. Am. Chem. Soc. 2012, 134, 14710–14713. [PubMed: 22928636]

(89). Mirica LM; Ottenwaelder X; Stack TD Structure and spectroscopy of copper-dioxygen complexes. Chem. Rev. 2004, 104, 1013–1045. [PubMed: 14871148]

(90). Company A; Palavicini S; Garcia-Bosch I; Mas-Balleste R; Que L Jr.; Rybak-Akimova EV; Casella L; Ribas X; Costas M Tyrosinase-like reactivity in a Cu(III)2(μ-O)2 species. Chem. - Eur. J. 2008, 14, 3535–3538. [PubMed: 18348133]

(91). Serrano-Plana J; Garcia-Bosch I; Miyake R; Costas M; Company A Selective ortho-hydroxylation-defluorination of 2-fluorophenolates with a bis(μ-oxo)dicopper(III) species. Angew. Chem., Int. Ed. 2014, 53, 9608–9612.

(92). Olivos Suarez AI; Jiang H; Zhang XP; de Bruin B The radical mechanism of cobalt(II) porphyrin-catalyzed olefin aziridination and the importance of cooperative H-bonding. Dalton Trans. 2011, 40, 5697–5705. [PubMed: 21483935]

(93). Bour JR; Camasso NM; Sanford MS Oxidation of Ni(II) to Ni(IV) with Aryl Electrophiles Enables Ni-Mediated Aryl-CF_3 Coupling. J. Am. Chem. Soc. 2015, 137, 8034–8037. [PubMed: 26079544]

(94). Wolczanski PT Flipping the Oxidation State Formalism: Charge Distribution in Organometallic Complexes As Reported by Carbon Monoxide. Organometallics 2017, 36, 622–631.

(95). Pauling L General Chemistry, 3rd ed.; Dover: New York, 1988; p 192.

(96). Pauling L The Modern Theory of Valency. J. Chem. Soc. 1948, 1461–1467. [PubMed: 18893624]

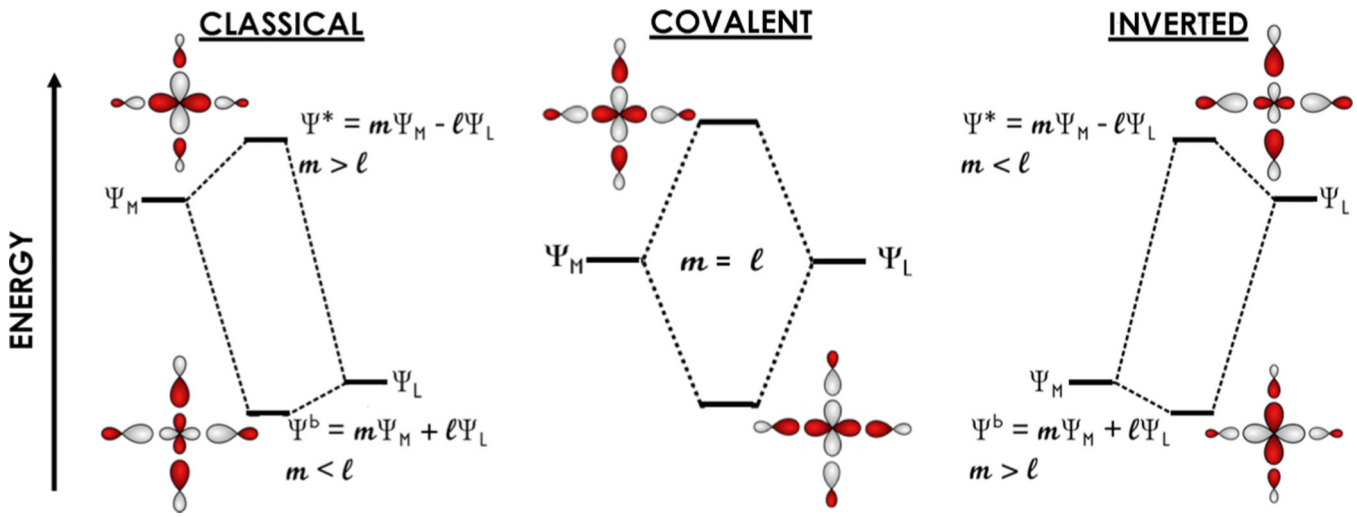

Figure 1.

Ligand field molecular orbital (MO) bonding regimes, ranging from a classical Werner-type field in which the frontier unoccupied Ψ* MO is characterized by predominantly metal-centered 3d-character (left), a covalent regime in which the M−L bond receives equal contribution from the metal 3d orbitals and ligand orbitals (middle), and an inverted ligand field in which Ψ* has predominantly ligand orbital character (right).

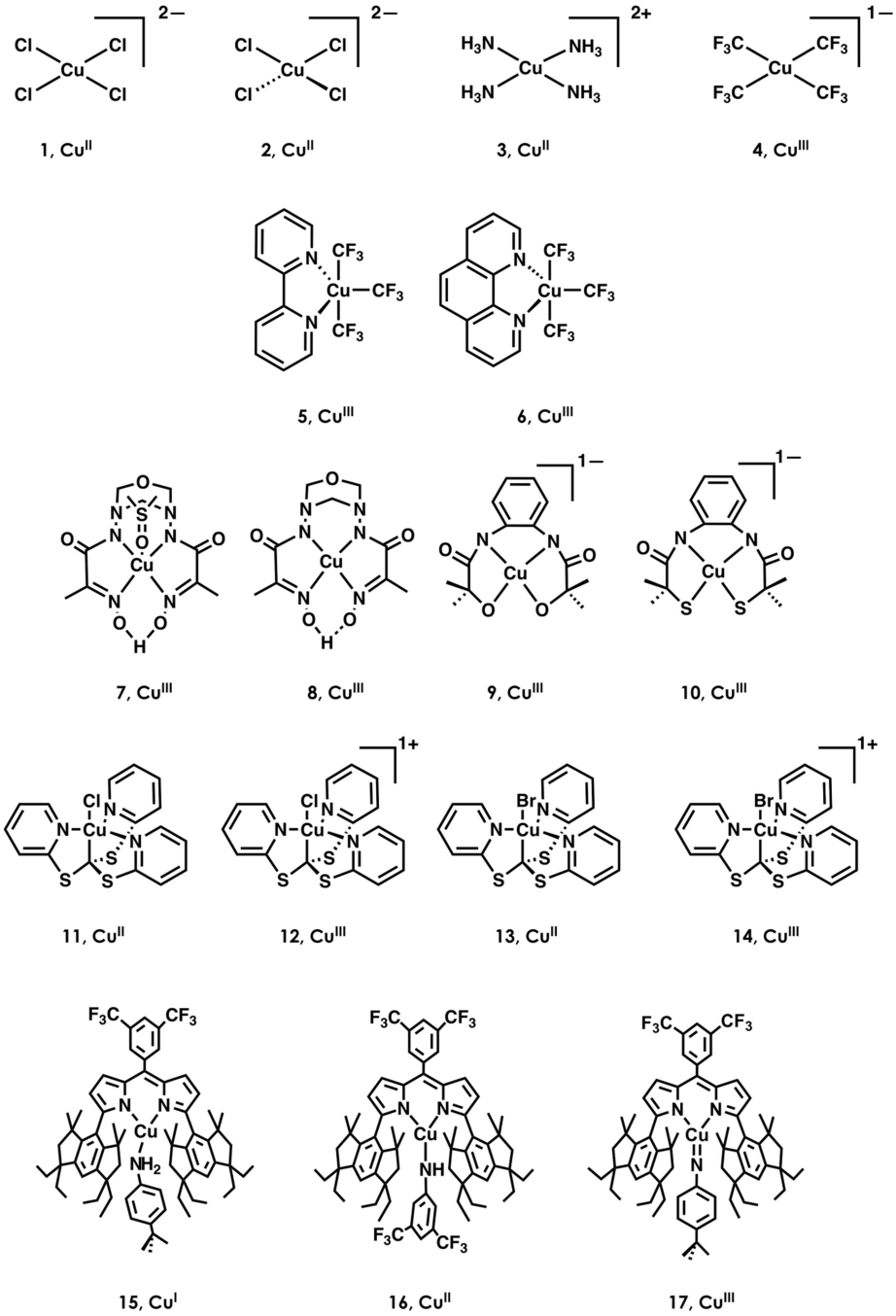

Figure 2.

Cu complexes investigated in this study. Formal oxidation states are shown below each complex.

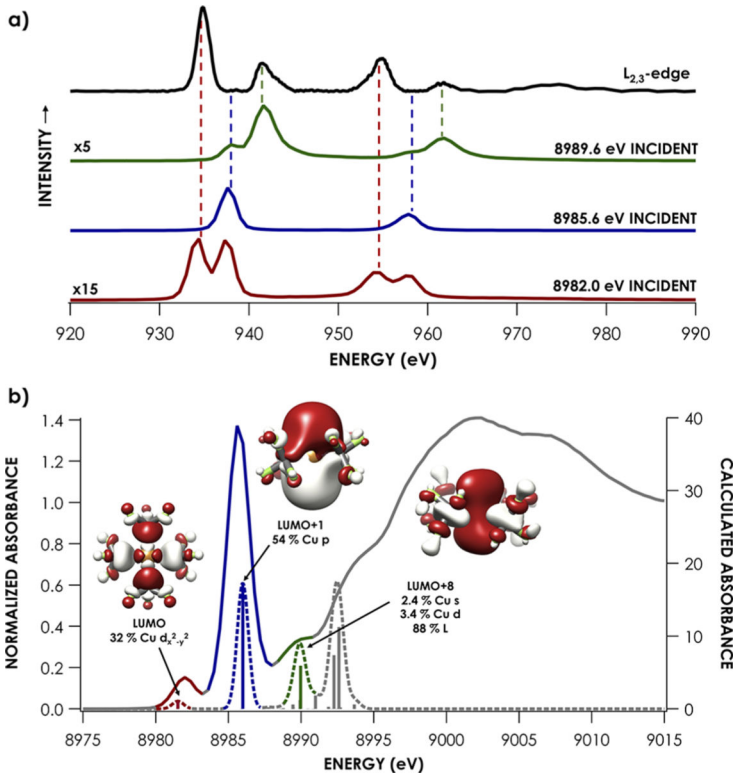

Figure 3.

(a) $L_{2,3}$-edge mainline (black) of **4** and RIXS energy-transfer slices corresponding to incident excitation at 8989.6 eV (green), 8985.6 eV (blue), and 8982.0 eV (red). (b) Corresponding experimental HERFD Cu K-edge XAS spectra (solid) and TDDFT-calculated (B3LYP, CP(PPP) on Cu, ZORA-def2-TZVP(-f) on all other atoms) Cu K-edge XAS (dashed) highlighting acceptor MOs accessed at 8982.0 eV (red), 8985.6 eV (blue), and 8989.6 eV (green). 1s2p RIXS energy-transfer data in (a) are reproduced from ref 14.

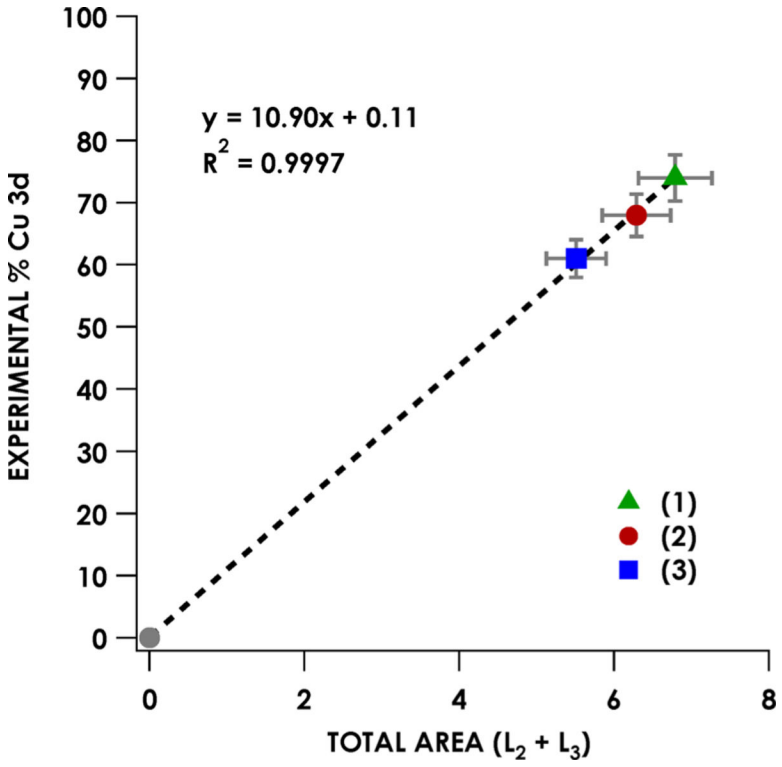

Figure 4.

Correlation between summed $L_{2,3}$-edge area of **1**−**3** and Cu 3d contribution to acceptor molecular orbitals. Error in the slope is estimated at ±0.14, and the error in the intercept is estimated at ±0.6.

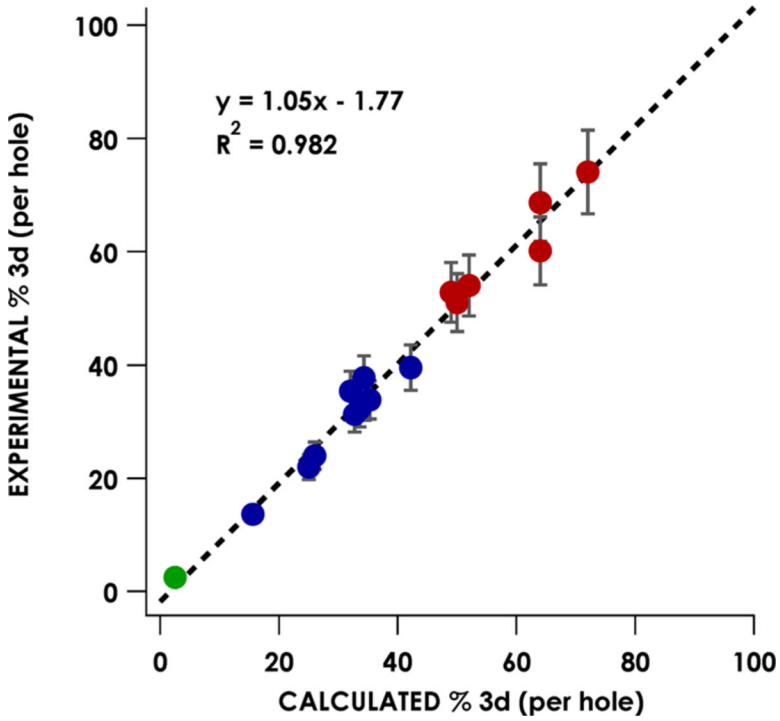

Figure 5.

Correlation between experimental and calculated Cu d-character in $L_{2,3}$-edge acceptor MOs for formally Cu^{II} (red), Cu^{III} (blue), and Cu^{I} (green) species. Error in the slope is estimated at ±0.04, and error in the intercept is estimated at ±1.55.

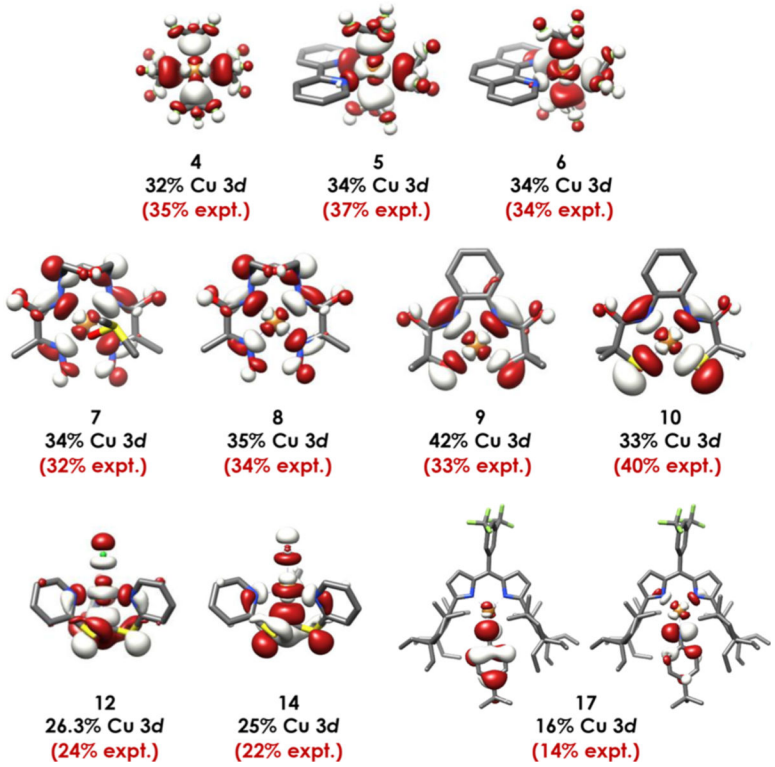

Figure 6.

LUMOs (**4**−**10**, **12**, and **14**) and SOMOs (**17**) of formally Cu^{III} species. Experimental (red) and calculated (black) % Cu 3d contributions are given, showing that ligand field inversion is operative in all cases. Orbitals shown are the QROs plotted at an isolevel of 0.03 au.

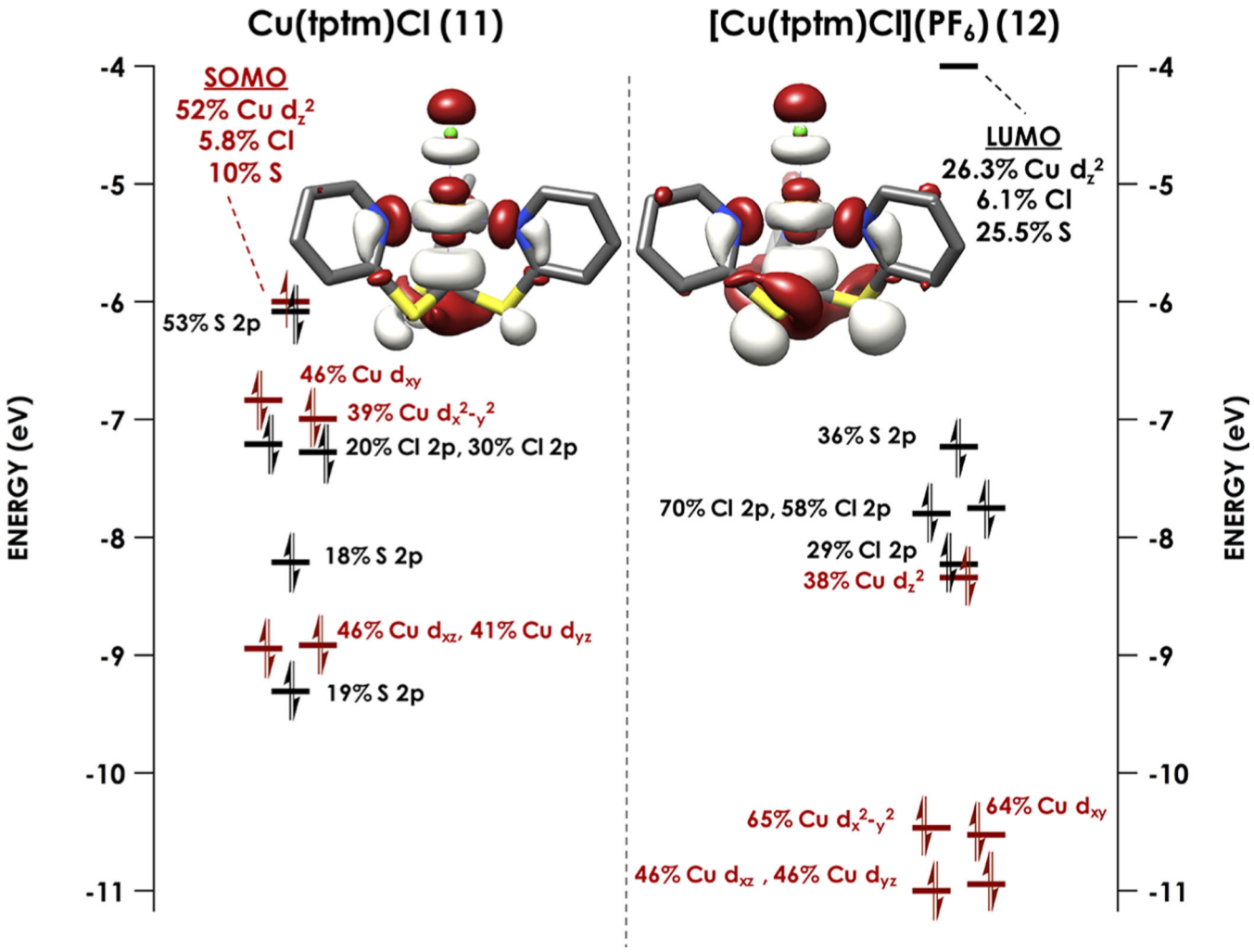

Figure 7.

Frontier MO diagrams (calculated using B3LYP with CP(PPP) on Cu and ZORA-def2-TZVP(-f) on all other atoms) corresponding to 11 (left) and 12 (right). Cu-localized orbitals are shown in red, and the ligand-localized MOs are shown in black; both are plotted at an isolevel of 0.03 au.

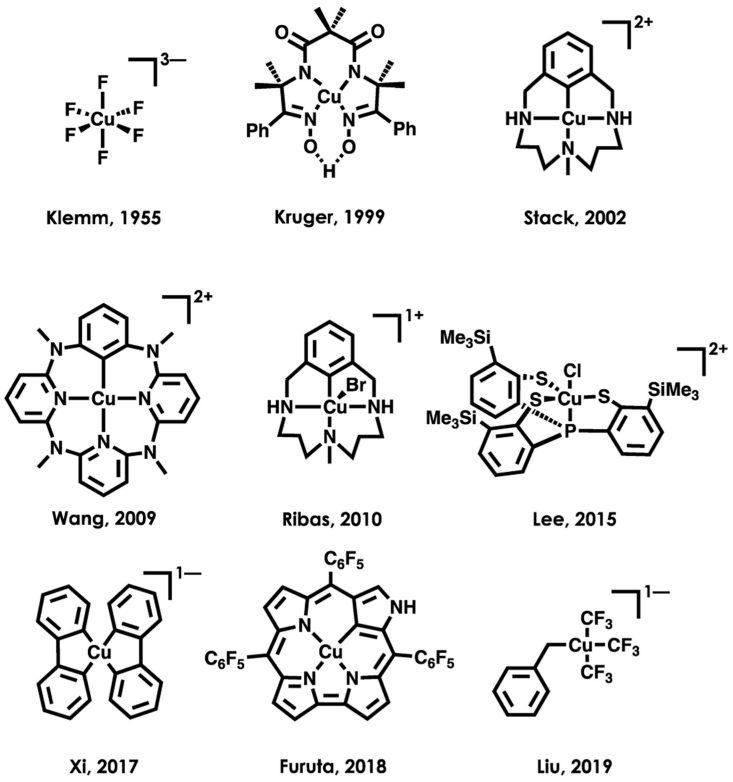

Figure 8.
Sampling of additional previously reported, stable Cu^{III} complexes spanning a range of geometries and ligand compositions.

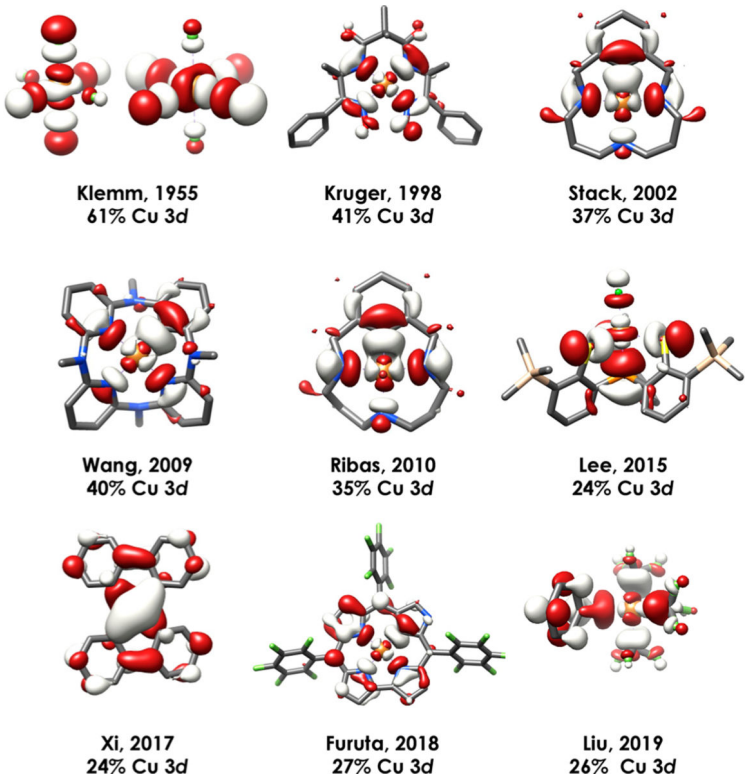

Figure 9.

DFT calculated frontier LUMO orbitals along with corresponding Löwdin orbital composition for reported Cu^{III} compounds shown in Figure 8. Unrestricted Kohn−Sham α MOs plotted at an isolevel of 0.03 au.

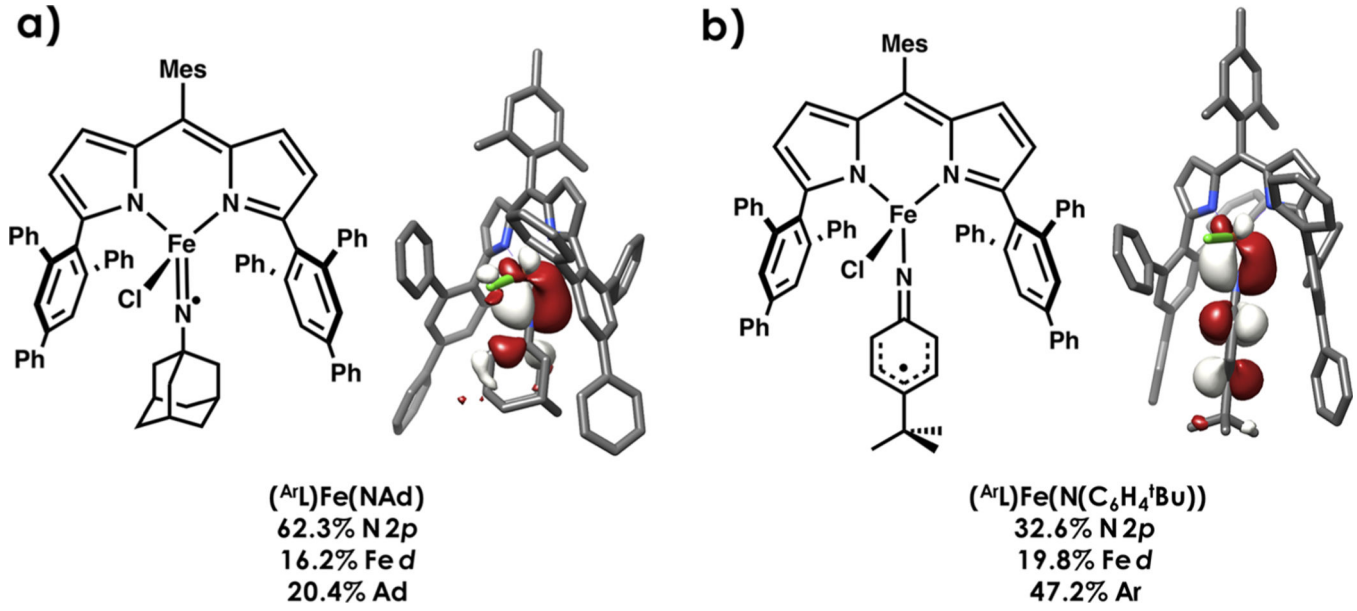

Figure 10.

DFT-calculated frontier molecular orbitals of (a) **17** and (b) $[(L^{TEED}Cu)_2(O_2)]^{2+}$ highlighting large N 2p and O 2p orbital contribution to the SOMOs, respectively. QRO orbitals are plotted at an isolevel of 0.03 au.

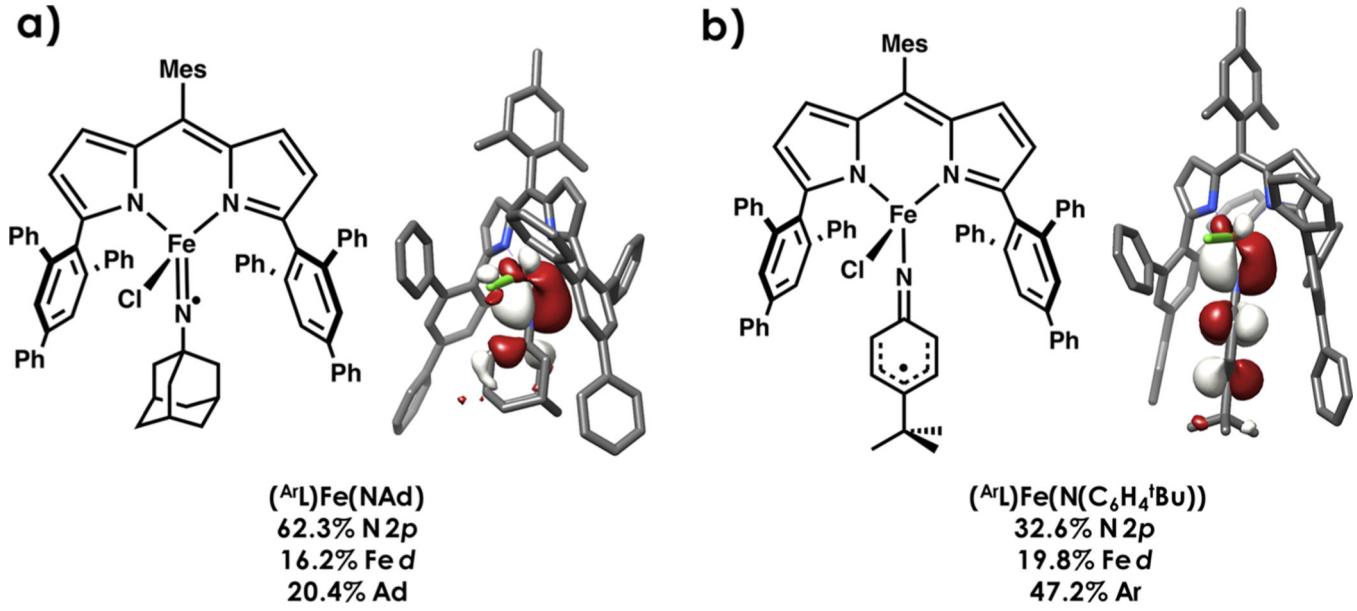

Figure 11.

DFT-calculated frontier molecular orbitals of (a) (^{Ar}L)Fe(NAd) and (b) (^{Ar}L)Fe(N(C_6H_4 ^{t}Bu)) highlighting large N 2p orbital contribution in the β SOMO, respectively. Unrestricted corresponding orbitals (UCOs) are plotted at an isolevel of 0.03 au.

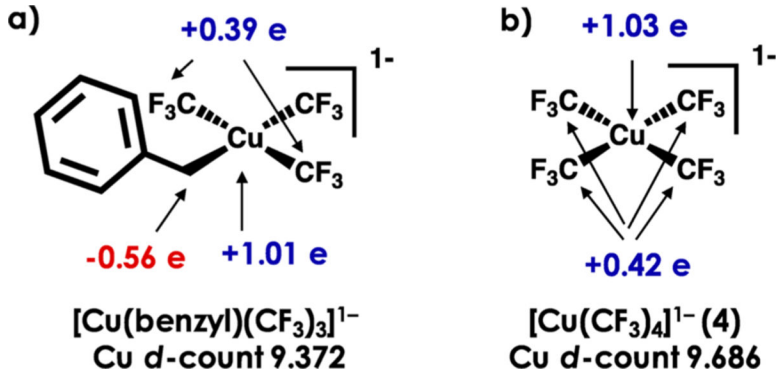

Figure 12.

Charge on bound C's in $[Cu(benzyl)(CF_3)_3]^{1-}$ and $[Cu(CF_3)_4]^{1-}$. Cu 3d counts obtained Löwdin population analyses following hybrid DFT single point using the B3LYP functional, CP(PPP) basis on Cu, and ZORA-def2-TZVP(-f) on all other atoms. C-atom charges (indicated by arrows) were obtained from IBBA analysis of the aforementioned single-point calculations.

Table 1.

Tabulated Experimental and TDDFT Calculated (B3LYP)[a] Cu K-Edge Pre-edge and Rising-Edge Features for Compounds 1−17

compound	experimental pre-edge energy (eV)	corrected calculated pre-edge energy (eV)	experimental edge feature energy (eV)	corrected calculated edge feature energy (eV)
1	8977.6	8977.9		
2	8979.1	8978.4	8985.9	8985.8
3	8979.1	8979.1	8988.3	8988.4
4	8981.8	8981.2	8985.6	8985.6
5	8980.6	8980.8	8985.8	8986.3
6	8980.3	8980.8	8985.8	8986.3
7	8980.8	8980.7	8983.5	8984.0
8	8979.6	8980.4	8983.3	8983.9
9	8981.0	8980.8	8988.0	8987.0
10	8981.0	8980.5	8986.5	8986.5
11	8979.2	8978.8		
12	8979.2	8978.7		
13	8979.6	8979.8		
14	8979.6	8979.9		
15			8983.1	8983.0
16	8979.1	8978.8	8984	8982.5
17	8980.1	8981.1		

[a]TDDFT calculated energies shifted according to equation from correlation in Figure S18: corrected calculated energy = (0.889 × calculated energy) + 988 eV. Error in slope is estimated as 0.03, and error in intercept is estimated as 266 eV.

Table 2.

Experimental Cu $L_{2,3}$-Edge Energies, DFT-ROCIS Calculated (B3LYP) $L_{2,3}$-Edge Energies,[a] Experimental Acceptor Orbital Cu 3d Contributions, and Calculated Acceptor Orbital Cu 3d Contributions[b] for Compounds 1−17

compound	experimental L_3 maximum (eV)	experimental L_2 maximum (eV)	corrected calculated L_3 maximum (eV)	corrected calculated L_2 maximum (eV)	L_2+L_3 area	# of holes	experimental % Cu 3d per hole	calculated % Cu 3d per hole
1	930.5	950.1	929.2	948.9	6.79	1	74	72
2	930.9	950.7	930.0	949.8	5.51	1	60	64
3	931.1	950.7	930.4	950.2	6.29	1	69	64
4	934.7	954.7	934.7	954.4	6.48	2	35	32
5	933.5	953.3	934.3	953.9	6.15	2	34	34
6	933.9	952.8	934.3	954.0	6.92	2	37	34
7	932.7	952.7	933.7	953.4	5.92	2	32	34
8	932.7	952.5	934.1	953.8	6.20	2	34	35
9	933.9	953.7	934.1	953.6	5.73	2	33	31
10	934.1	953.4	934.0	953.6	7.24	2	40	42
11	930.6	950.5	930.3	950.0	4.95	1	54	52
12	931.2	950.6	932.6	950.1	4.47	2	24	26
13	930.6	950.2	930.3	950.1	5.98	1	51	50
14	930.3	951.1	930.3	952.3	4.04	2	22	25
15[c]	931.2	950.9	933.5	948.7	0.43	2	2.5	2.5
16	931.5	951.1	930.3	950.1	4.84	1	53	51
17[d]	932.1	951.9	930.6	950.7	2.49	2	14	16

[a] DFT-ROCIS calculated energies shifted according to equation from correlation in Figure S37; corrected calculated peak energy = 1.006 × (calculated peak energy) + 6.0 eV. Error in slope is estimated as 0.02, and error in intercept is estimated as 15 eV.

[b] Calculated acceptor orbital 3d contributions obtained by Löwdin population analysis of UKS orbitals subjected to QRO transformation. All calculations employed the B3LYP hybrid density functional with the CP(PPP) basis set on Cu and ZORA-def2-TZVP(-f) basis on all other atoms.

[c] Estimated from excitation into high-lying, doubly unoccupied MO of predominantly ligand parentage.

[d] Calculated acceptor orbital 3d contribution is the average % Cu 3d of each SOMO.